# Kerr, Faraday, and magnetoelectric effects in $MnBi_2Te_4$ thin films

Chao Lei* and Allan H. MacDonald
*Department of Physics, The University of Texas at Austin, Austin, Texas 78712, USA*

(Received 2 April 2023; accepted 8 September 2023; published 19 September 2023)

The topological magnetoelectric effect (TME) is a characteristic property of topological insulators. In this paper, we use a simplified coupled-Dirac-cone electronic structure model to theoretically evaluate the THz and far infrared Kerr and Faraday responses of thin films of $MnBi_2Te_4$ with up to $N = 10$ septuple layers with the goal of clarifying the relationship between these convenient magnetooptical observables and the TME. We find that for even $N$, the linear Kerr and Faraday responses to an electric field vanish in the low-frequency limit, even though the magnetoelectric response is large and approximately quantized.

DOI: 10.1103/PhysRevB.108.125424

## I. INTRODUCTION

Three-dimensional topological insulators (TIs) [1,2] have protected surface states with Dirac band crossings located at time-reversal invariant two-dimensional momenta and characteristic topological magnetoelectric (TME) response [3–8] properties. The TME effect occurs only when the Dirac cones are gapped by introducing magnetic dopants at the surface or by using magnetic TIs like $MnBi_2Te_4$, and has been proven to be difficult to measure directly [9,10]. In the thin-film limit, Kerr and Faraday's optical response coefficients and orbital magnetization, all of which require broken time-reversal symmetry, are closely related quantities that are normally present or absent together. Partly for this reason there has been interest [11–21] in using magneto-optical Kerr or Faraday effects as a proxy for magnetization since Kerr and Faraday effect measurements are routinely used as a proxy for magnetization measurements.

The Kerr and Faraday effects of TIs are easily measured [22–26] when external fields are applied or the magnetization orientations on top and bottom surfaces are parallel, in which case the device Hall conductivity is quantized [27–29] at a nonzero value and the magnetization is nonzero even in the absence of an electric field. $MnBi_2Te_4$ films with an odd number of septuple layers $N$ in which the surface magnetizations are parallel provide one example of this quantum Hall case. In this paper, we exclude the quantum Hall devices from consideration and focus on the case of even $N$ magnetic TIs (and on even-layer $MnBi_2Te_4$, in particular) instead of surface magnetized nonmagnetic TIs, since these seem at present to have more reproducible magnetic properties, although our conclusions apply to both cases.

Our interest here is thus in the magnetization response to electric field in $MnBi_2Te_4$ films with an even number of septuple layers, in which the TME coefficient is quantized and the total Hall conductivity in the absence of electric and magnetic field is zero. We point out that in this case both the Kerr and the Faraday responses to an electric field differ qualitatively from the magnetization response. Specifically for even $N$, the Kerr and Faraday angle response to an electric field vanishes at low frequencies under circumstances where the TME is robust. We explain this difference using a simplified coupled Dirac-cone model [30] of magnetic TI $MnBi_2Te_4$. Below we first explain the origin of this difference, and then explore it quantitatively using a simplified model of magnetic TI thin films.

## II. FARADAY, KERR, AND MAGNETOELECTRIC RESPONSE

Hall effects in two-dimensional insulators can be viewed [31] as measurements of the chemical potential dependence of equilibrium edge currents, $dI_{\rm edge}/d\mu = \sigma e/h$ or, equivalently, of the orbital magnetizations that they produce $dM_{\rm edge}/d\mu = \sigma A e^2/h$, where $e$ is the magnitude of the electron charge, $h$ is Plank's constant, $\sigma$ is an integer and A is the film area. In topological insulator thin films, $\sigma$ can be nonzero only when time-reversal symmetry is broken, either at the top and bottom surfaces or, as in the case of a magnetic topological insulator [32], throughout the bulk. In a system with A-type bulk antiferromagnetism, the TME occurs when opposite surfaces have opposite magnetizations, e.g., for an even number of magnetic layers. The magnetic configuration with opposite magnetization orientations on opposite surfaces is often referred to in the literature as the *axion insulator* configuration. Since the edge current at a surface depends only on the value of the chemical potential relative to the midgap energies of the local Dirac cones, or some other reference energy, it follows that $dM_{\rm edge}/dV_{\rm edge} = -dM_{\rm edge}/d\mu$. When an electric field is applied across the bulk of the topological insulator with thickness $t$, the local electrical potentials on the top and bottom surfaces differ by $e\mathcal{E}_z t$, moving the local Dirac bands relative to the chemical potential, as illustrated in Fig. 1. This difference yields a net magnetization that is linear in $\mathcal{E}_z$ and proportional to the system volume—the topological magnetoelectric effect. The total Hall conductivity of the axion insulator state, summing over top and bottom surfaces, still vanishes, however, provided that the chemical potential stays inside the surface state gap.

*leichao.ph@gmail.com

 

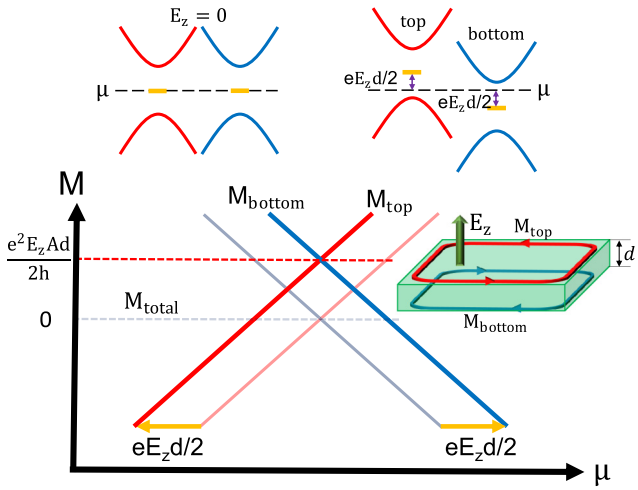


FIG. 1. Magnetization due to current circulating around the top (red) and bottom (blue) surfaces of a magnetic TI. At each surface, the magnetization depends linearly on the local chemical potential relative to the local electric potential. When an electric field $\mathcal{E}_z$ is applied across the bulk of the thin film, it produces a relative energetic shift between the gapped Dirac cones. The total equilibrium orbital magnetization is then proportional to $\mathcal{E}_z$ and the film volume.

The TME effect refers to the dc response properties of TIs, but is also approximately manifested at finite frequencies provided they are well below the TI bulk energy gap. Since the gaps of $MnBi_2Te_4$ thin films are usually less than 100 meV, typical film thicknesses $d$ are very small compared to the relevant light wavelength $\lambda$. (For example, $d \sim 150$ nm for a $N = 10$ septuple layer $MnBi_2Te_4$ thin film is small compared to the vacuum wavelength $\lambda \sim 25$ μm of 50 meV light.) In the thin film ($d \ll \lambda$) limit, we can calculate the Kerr and Faraday responses simply by treating the entire film as an arbitrarily thin two-dimensional interface. The response of light to currents in the 2D film is determined by the electromagnetic boundary condition:

$$\mathbf{n} \times (\mathbf{H}_t - \mathbf{H}_b) = \mathbf{j}_s. \tag{1}$$

Here $\mathbf{n}$ is a unit vector oriented from top to bottom and $j_s$ is the two-dimensional current density, which is related to the two-dimensional conductivity of the film by

$$j_s^\alpha = \sum_\beta \sigma_{\alpha\beta} E_\beta. \tag{2}$$

When Eq. (1) is combined with the source-free Maxwell's equations applied outside of the thin film, the in-plane transmitted and reflected fields produced by an incident *em* wave with an unit electric field are [11]

$$\begin{pmatrix} E_x^t \\ E_y^t \end{pmatrix} = \frac{1}{\mathcal{N}} \begin{pmatrix} 2n_1(n_1+n_2+2\alpha\sigma_{xx}) \\ -4\alpha n_1 \sigma_{xy} \end{pmatrix},$$
$$\begin{pmatrix} E_x^r \\ E_y^r \end{pmatrix} = \frac{1}{\mathcal{N}} \begin{pmatrix} n_1^2 - (n_2+2\alpha\sigma_{xx})^2 - (2\alpha\sigma_{xy})^2 \\ -4\alpha n_1 \sigma_{xy} \end{pmatrix}, \tag{3}$$

where $\sigma_{xx}$ and $\sigma_{xy}$ are the total longitudinal and Hall conductivities of the film in units of $e^2/h$, $\alpha \approx 1/137$ is the fine structure constant, $\mathcal{N} \equiv (n_1+n_2+2\alpha\sigma_{xx})^2 + (2\alpha\sigma_{xy})^2$, and $n_i^2 = \epsilon_i$ are the relative dielectric constants of the materials above and below the interface. The 2D film conductivities should be evaluated by integrating across the film and include contributions from both dissipative and reactive responses of the TI film both at its surfaces and in the interior of the film. The 2D approximation, which has the advantage of allowing us to reach simple conclusions, is strictly speaking valid only in the limit $d/\lambda \to 0$, as discussed further below.

The Faraday and Kerr angles are defined, respectively, as the rotation angles of linearly polarized incoming light upon transmission and reflection,

$$\theta_F = (\arg E_+^t - \arg E_-^t)/2,$$
$$\theta_K = (\arg E_+^r - \arg E_-^r)/2, \tag{4}$$

where $E_\pm^{r/t} \equiv E_x^{r/t} \pm iE_y^{r/t}$. Here the values of incoming in-plane polarization can be read from Eq. (3).

For even $N$ films, both the Hall conductivity and the magnetization vanish by symmetry [33,34] in the absence of external out-of-plane electric field $\mathcal{E}_z = 0$ at all frequencies. Because of quantization, the dc Hall conductivity vanishes identically at finite $\mathcal{E}_z$ until the field is strong enough to close the gap. The linear response of the Hall conductivity to $\mathcal{E}_z$ is therefore zero in the dc limit. Under the same conditions, the linear response of the magnetization is quantized at the topologically protected value. We anticipate that the linear response of the Kerr and Faraday effects to external electric field $E_z$ is strongly suppressed when $\hbar\omega$ is well below the band gap of $MnBi_2Te_4$ thin films. In the following, we use a simplified model to test this expectation quantitatively.

## III. OPTICAL CONDUCTIVITY OF MBT THIN FILMS

We evaluate the frequency-dependent conductivity tensor of $MnBi_2Te_4$ [30,35–49] thin films using a coupled-Dirac-cone model [30] that retains two Dirac cones in each $MnBi_2Te_4$ septuple layer as low-energy degrees of freedom. The full Hamiltonian in the presence of external out-of-plane electric field reads [50]

$$H = \sum_{\mathbf{k}_\perp, ij} [((-)^i \hbar v_D (\hat{z} \times \sigma) \cdot \mathbf{k}_\perp + m_i \sigma_z + V_i)\delta_{ij}$$
$$+ \Delta_{ij}(1-\delta_{ij})] c_{\mathbf{k}_\perp i}^\dagger c_{\mathbf{k}_\perp j}. \tag{5}$$

Here the Dirac cone labels $i$ and $j$ are, respectively, odd and even on the top and bottom surface of each septuple layer, $\hbar$ is the reduced Planck's constant, $v_D$ is the Dirac-cone velocity, and $V_i = V_{i-1} + \mathcal{E}_i(z_i - z_{i-1})$ is the self-consistent Hartree potential on surface $i$, with $z_i$ the designed position of the $i$th Dirac cone. The external electric field is calculated with discrete Poisson equation as $\tilde{\epsilon}\mathcal{E}_i = \tilde{\epsilon}\mathcal{E}_{i-1} + \delta\rho_i$, here $\tilde{\epsilon}$ is the dielectric constant, and $\delta\rho_i$ are the net surface charge densities at surface $i$; more details for the calculations of $\delta\rho_i$ and related parameters can be found in Ref. [50]. In the following discussion, when the electric field is present, we will always consider the case when the Fermi level lies in the gap, i.e., we will keep the system neutral. The Dirac-cone model describes a TI when the hybridization $\Delta_D$ across the gap between different septuple layers is stronger than the hybridization $\Delta_S$ between top and bottom Dirac cones in the same septuple layer. Each Dirac cone has an exchange splitting $m$ that is the sum of contributions from the near-neighbor

Mn magnetic layers within the same ($J_S$) septuple layer and in the adjacent septuple layer ($J_D$). An $N$-septuple layer thin film is reduced by this model to a quasi-2D system with 4N bands. For the calculations we report on below, we use the numerical model parameters that provide a minimal description [30] of $MnBi_2Te_4$ thin films: Dirac velocity $v_D = 5\times10^5$ m/s, $\Delta_S = 84$ meV, $\Delta_D = -127$ meV, $J_S = 36$ meV, and $J_D = 29$ meV.

The optical conductivity of the Dirac cone model is calculated by using the Kubo-Greenwood formula [51,52],

$$\sigma_{\alpha\beta}(\omega) = \frac{ie^2}{\hbar}\int \frac{d\mathbf{k}}{(2\pi)^2}\sum_{nm}\frac{f_{n\mathbf{k}} - f_{m\mathbf{k}}}{E_{n\mathbf{k}} - E_{m\mathbf{k}}} \times \frac{\langle m\mathbf{k}|\partial_\alpha H_{\mathbf{k}}|n\mathbf{k}\rangle\,\langle n\mathbf{k}|\partial_\beta H_{\mathbf{k}}|m\mathbf{k}\rangle}{E_{n\mathbf{k}} - E_{m\mathbf{k}} - (\hbar\omega + i\eta)}, \tag{6}$$

where $\partial_\alpha H_{\mathbf{k}} \equiv \partial_{k_\alpha} H_{\mathbf{k}}$, $\omega$ is the optical frequency, $\hbar$ is the reduced Planck's constant, $\alpha, \beta = x, y$ are Cartesian tensor labels, $n, m$ are band indices, $|n\mathbf{k}\rangle$ is a Bloch state, $E_{n\mathbf{k}}$ is a band energy, $f_{n\mathbf{k}}$ is Fermi-Dirac band occupation probability, and $\eta$ is a disorder broadening parameter that is set to 0.5 meV. In the Dirac cone model [30], $\partial_x H_{\mathbf{k}} = \hbar v_D \sigma_y \tau_z$, $\partial_y H_{\mathbf{k}} = -\hbar v_D \sigma_x \tau_z$, where $\sigma_\alpha$ is a Pauli matrix acting on spin. The band energies in Eq. (6) depend only on the magnitude of wave vector $\mathbf{k}$, and the velocity matrix elements have a simple angle dependence that allows angular integrals to be performed analytically. Our calculations are therefore performed by integrating numerically over the radial direction of 2D k-space after performing the angular integrals analytically. Because we employ continuum Dirac models for the $\hat{x} - \hat{y}$ planes, the numerical integrals require a k-space cutoff. In our numerical calculations, we used an adaptive $k$-mesh with a higher density over the range of $k$ with a large Berry curvature, and a sparse mesh where the Berry curvature is small. In this specific model, the Berry curvatures are mainly contributed around $\mathbf{k} = 0$ and our $k$-mesh samplings are set as follows:

$$k \in \begin{cases} [0, 2^n]\frac{\pi}{a} & n = 0 \\ [2^{n-1}, 2^n]\frac{\pi}{a} & n = 1, 2, 3, \ldots, M. \end{cases} \tag{7}$$

Here $a$ is selected so the Berry curvature is concentrated in the range of $[0, \pi/a]$ and therefore depends on the band gap where band inversion appears. $M$ determines the cutoff of the wave vector. We normally set $M = 12$, which places any anomalies associated with the cutoffs outside of the range of frequencies that we plot.

In Fig. 2, we illustrate the main features of $\mathcal{E}_z = 0$ systems by plotting the band structure and frequency-dependent longitudinal and Hall optical conductivities [$\sigma_{xx}(\omega)$ and $\sigma_{xy}(\omega)$] of antiferromagnetic (AFM) $MnBi_2Te_4$ thin films with septuple-layer numbers $N = 4$ and $N = 5$ (The optical conductivities for other AFM thin films as shown in Fig. 8 of Appendix A). The ground states for $N = 4$ and other even-$N$ films are referred to as axion insulators in the literature and have similar conductivities. The $N = 5$ case is an example of an odd $N$ magnetic configuration that supports a quantum anomalous Hall effect and therefore does not have axion electrodynamics. The electronic structure of $N = 4$ thin film is invariant under combined time-reversal ($\mathcal{T}$) and inversion ($\mathcal{I}$) symmetry, which leads, via a generalized Kramer's theorem, to the doubly degenerate 2D bands [33] shown in Fig. 2(a). In this case, as shown in Fig. 2(b), both real (red solid curve) and

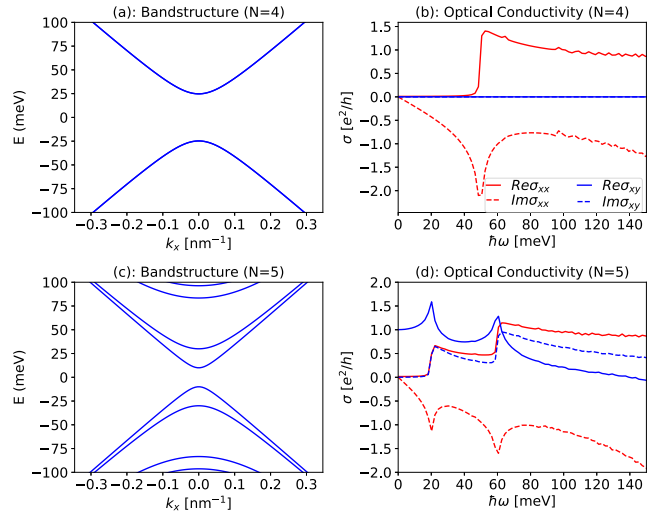


FIG. 2. Band structure and optical conductivity for antiferromagnetic $MnBi_2Te_4$ thin films with septuple layer numbers $N = 4, 5$. (a) Band structure of $N = 4$ $MnBi_2Te_4$ along $x$ direction of the momentum, with $k_y$ to be zero since the Hamiltonian is rotational invariant. Even-$N$ bands are doubly degenerate due to the $\mathcal{TI}$ symmetry discussed in the text. (b) Two-dimensional optical conductivity versus frequency of $N = 4$ $MnBi_2Te_4$. The Hall conductivity vanishes identically due to $\mathcal{TI}$ symmetry. (c), (d) Band structure and conductivity plots for $N = 5$ $MnBi_2Te_4$, which has a quantum anomalous Hall effect. The dc limit of the Hall conductivity is therefore quantized. Longitudinal conductivities ($\sigma_{xx}$) are plotted in red and Hall conductivities ($\sigma_{xy}$) in blue. In each case, the real and imaginary parts are plotted as solid and dashed lines. All conductivities are expressed in units of $e^2/h$.

imaginary (dashed red curve) parts of longitudinal conductivity ($\sigma_{xx}$) approach 0 in the low-frequency limit and have interband features at ≈50 meV. The Hall conductivity ($\sigma_{xy}$), and therefore both Kerr and Faraday angles, vanish identically over the entire range of frequencies due to $\mathcal{TI}$ symmetry. For thin films with an odd number of layers, there is no $\mathcal{TI}$ symmetry and the band degeneracy is lifted as shown in Fig. 2(c). AFM $MnBi_2Te_4$ thin films with thickness $N > 3$ are Chern insulators with Chern number $C = 1$ and therefore have quantized dc Hall conductivities as shown in Fig. 2(d). The gap of the $N = 5$ Chern insulator is small (∼20 meV) because the minimum thickness necessary for Hall quantization is only modestly exceeded [50]. In Fig. 9 of Appendix A, we summarize the properties of the conductivity tensor in thin films with spin-aligned magnetic configurations, which can be induced in $MnBi_2Te_4$ by applying magnetic fields exceeding ∼5 Tesla [37,41,42]. Based on these optical conductivities, the corresponding Kerr and Faraday rotations versus optical frequencies of $MnBi_2Te_4$ thin films are estimated as shown in Fig. 3; here we estimate the magneto-optical rotation angles in the 2D limit. The Faraday and Kerr rotations for AFM thin films are shown in Figs. 3(a) and 3(c), from which we see that for thin films with even-number layers (corresponds to dashed curves), there is no Faraday and Kerr signals as $\sigma_{xy}(\omega) = 0$. For odd-$N$ thin films, however, there is a large Faraday and Kerr rotation angle ($\theta_{F/K}$) at finite frequencies even though the $MnBi_2Te_4$ thin films are trivial insulators; see $N = 1$ or

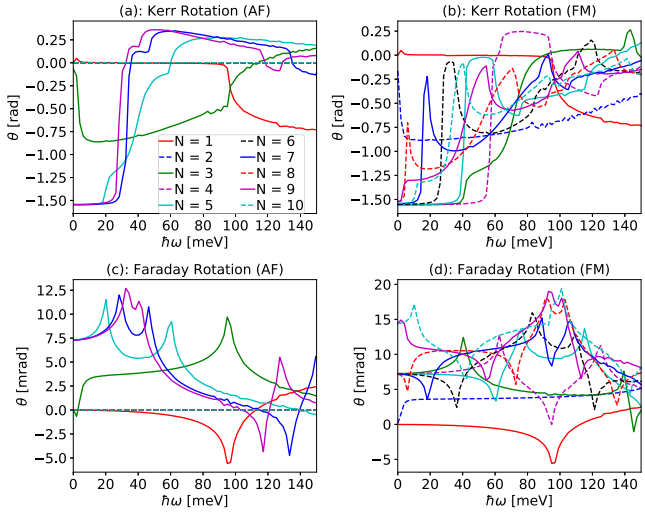


FIG. 3. Kerr and Faraday rotation angle versus optical frequency. (a), (b) Plots of Faraday rotation angles of $MnBi_2Te_4$ thin films in AFM and FM states. (b) Faraday rotation angles of $MnBi_2Te_4$ thin films in FM state. (c), (d) Plots of Kerr rotation angles of $MnBi_2Te_4$ thin films in AFM state; (d) Kerr rotation angles of $MnBi_2Te_4$ thin films in FM state. In these plots, the same color labels the same thickness of $MnBi_2Te_4$ thin films in all four panels.

$N = 3$ thin films, for example, although $\theta_{F/K}$ is still 0 in the dc limit. When the thin films are in Chern insulator states, the Faraday and Kerr rotation angles in the dc limit approach the quantized value, i.e., $-\tan^{-1}(1/4\pi \mathrm{Re}\sigma_{xy}) \approx -\pi/2$ for the Kerr rotation angle; and $\tan^{-1}(4\pi \mathrm{Re}\sigma_{xy}) = C\tan^{-1}\alpha$ for the Faraday rotation angle. Here $C$ is the Chern number and $\alpha$ is the fine structure constant.

## IV. ELECTRIC-FIELD DEPENDENCE OF THE FARADAY AND KERR ANGLES

The $\mathcal{TI}$ symmetry that causes the Kerr, Faraday, and orbital magnetization responses to simultaneously vanish in axion insulator states is broken by an electric field $\mathcal{E}_z$ applied across the film. Based on the Schrödinger-Poisson equation, we calculate the orbital magnetoelectric response for MBT thin films with the modern theory of orbital magnetization, which leads to the following expression [53–56]:

$$M_{\mathrm{orb}} = \frac{e}{2\hbar}\int \frac{1}{(2\pi)^2} d\mathbf{k} \sum_n f_{n\mathbf{k}} \mathrm{Im}\langle \partial_{\mathbf{k}} \mathrm{u}_{\mathbf{nk}}| \times (H_{\mathbf{k}} + E_{n\mathbf{k}} - 2\mu)|\partial_{\mathbf{k}} u_{n\mathbf{k}}\rangle, \quad (8)$$

where $f_{n\mathbf{k}}$ is the Fermi-Dirac distribution function, $H_{\mathbf{k}}$ is the Hamiltonian introduced in Eq. (5), $E_{n\mathbf{k}}$ is the eigenvalue of the $nth$ subbands, $\mu$ is the chemical potential, and the wave-vector integrals are over two-dimensional momentum space. The orbital magnetism response to $\mathcal{E}_z$ (denoted as $\mathcal{E}$ in the plots since we consider the electric field only in the $z$ direction), plotted as blue curves in Figs. 4(a) and 4(b), is initially linear with small finite thickness corrections [57] to the quantized response coefficient, which is common to all TIs. This topological response is strong, at least compared to that of typical magnetoelectric materials like $Cr2O_3$.

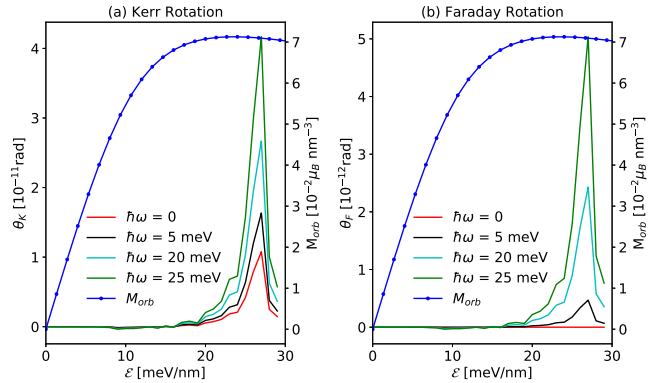


FIG. 4. Comparison of the electric field ($\mathcal{E}$, corresponding to $\mathcal{E}_z$ in the main text) dependence of the orbital magnetization, and the Kerr (a) and Faraday (b) rotation angles for antiferromagnetic $MnBi_2Te_4$ thin films with a thickness of $N = 4$ septuple layers. In this figure, the Kerr and Faraday angles are calculated in 2D limit in which the film thickness is very small compared to the light wavelength.

We now combine the simplified coupled Dirac cone model and self-consistent Schrödinger-Possion equations [50] to model the effect of $\mathcal{E}_z$ on the magneto-optical response. In Figs. 4(a) and 4(b), we show typical 2D limit Kerr and Faraday rotation angles for even-layer thin films calculated from the conductivity tensor of an $N = 4$ axion insulator thin film using a substrate dielectric constant $n_s = 1$. We see that the Kerr and Faraday angles have extremely small linear response coefficients and that they remain small even when the vertical electric field $\mathcal{E}_z$ [50] is near the critical value at which the film gap vanishes. We attribute these very small values to the approximate locality of the Hall response at top and bottom surfaces. Because the surface magnetizations are opposite, the total Hall conductivities nearly vanish at all frequencies even for $\mathcal{E}_z \neq 0$. The Kerr and Faraday angles in Fig. 4 ($\sim 10^{-11}$ rad) lie below current Kerr angle detection limits [58,59] to the best of our knowledge. The frequency and electric field dependence of the underlying conductivities is presented in Figs. 10–12 of Appendix B. Because these response coefficients calculated in the 2D limit are practically zero even at $\mathcal{E}_z \neq 0$, the finite thickness corrections we examine next are actually dominant.

## V. THICKNESS DEPENDENCE

Because the Kerr response is so weak in the 2D limit, finite thickness corrections can easily be important. To assess the film thickness dependence of the Kerr and Faraday response, we first model the thin film as two Dirac surfaces that support half-quantized Hall effects of opposite signs and are separated by a dielectric bulk. The electromagnetic wave then scatters at both interfaces. Denote the incoming field as $[\tilde{E}^{ti} \;\; \tilde{E}^{ri}]^T$ and outgoing field as $[\tilde{E}^{ri} \;\; \tilde{E}^{tj}]^T$, at the interface the incoming and outgoing fields are connected with the scattering matrix $S$ which reads

$$S = \begin{pmatrix} \bar{r} & \bar{t}' \\ \bar{t} & \bar{r}' \end{pmatrix}, \quad (9)$$

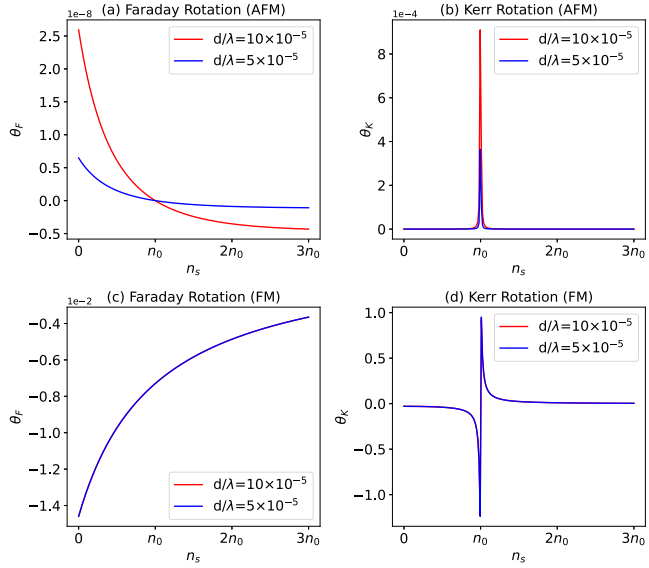


FIG. 5. Dependence of magneto-optical Faraday and Kerr rotation angles versus the relative dielectric constant of the substrate. (a), (b) Dependence of Faraday/Kerr rotation angles on relative dielectric constant of substrate for AFM states; (c), (d) plots for FM state.

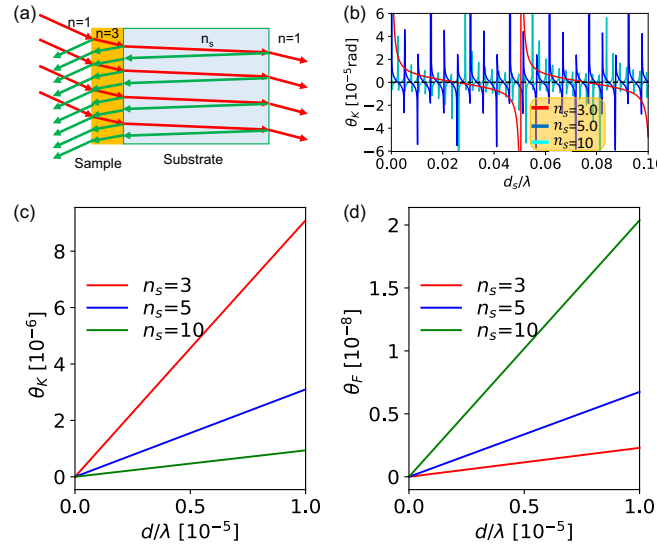


FIG. 6. (a) Illustration of light reflection and transmission for a finite-thickness film with a substrate. (b) Kerr rotation versus substrate thickness $d_s$ for various substrate dielectric constants. These results were calculated for a light frequency of 25 meV, which is below the gap at $\mathcal{E}_z = 0$, an electric field $\mathcal{E}_z = 25$ meV/nm, which is close to but smaller than the critical electric field for gap closure, and a $N = 4$ septuple layer sample thickness. (c), (d) Dependence of Kerr and Faraday angles on sample thickness at $\mathcal{E}_z = 0$ with the substrate thickness set to $d = 200\lambda$. The range of thickness to wavelength ratio corresponds to photon energies ∼10 meV and films with fewer than ∼10 septuple layers.

Here $\bar{r}'$ and $\bar{t}'$, the reflection and transmission tensors for incidence from the right, are obtained from $\bar{r}$ and $(\bar{t})$ by reversing the wave-vector direction and interchanging the dielectric constants on opposite sides of the interface [11]. $\bar{r}$, $\bar{t}$ are defined as

$$\bar{r} = \begin{pmatrix} r_{xx} & r_{xy} \\ -r_{xy} & r_{yy} \end{pmatrix}, \quad \bar{t} = \begin{pmatrix} t_{xx} & t_{xy} \\ -t_{xy} & t_{yy} \end{pmatrix}.$$

This total reflection and transmission tensors $\bar{r}$ and $\bar{t}$ can be composed from the top ($T$) and bottom ($B$) single-interface scattering matrices:

$$\bar{r} = \bar{r}_T + \bar{t}'_T \bar{r}_B (1 - \bar{r}'_T \bar{r}_B)^{-1} \bar{t}_T, \quad \bar{t} = \bar{t}_B (1 - \bar{r}'_T \bar{r}_B)^{-1} \bar{t}_T. \quad (10)$$

The resulting Kerr and Faraday rotations depend strongly on the dielectric constants experienced by incoming and outgoing light. If we assume that light is incoming from vacuum with relative dielectric constant ($n_0 = 1$) and is outgoing to an infinite substrate with relative dielectric constant $n_s$, the Faraday rotation angle for an AFM thin film is nonzero only when $n_s \neq 1$. In contrast, the Kerr rotation angle is nonzero when $n_s = n_0$, as illustrated in Figs. 5(a) and 5(b). In Figs. 5(c) and 5(d), the Kerr and Faraday rotation angles for thin films with a ferromagnetic (FM) state are plotted.

When the thickness of substrates is considered to be finite, i.e., with substrate thickness $d_s$, We can account for both the thickness and the index of refraction ($n_s$) of the substrate by replacing $\bar{t}_B$ and $\bar{r}_B$ by $\bar{t}_S$ and $\bar{r}_S$, which can be calculated by composing two single-interface scattering matrices—in this case, the interfaces between substrate and sample and between substrate and vacuum,

$$\bar{r} = \bar{r}_T + \bar{t}'_T \bar{r}_{SB} (1 - \bar{r}'_T \bar{r}_{SB})^{-1} \bar{t}_T, \quad \bar{t} = \bar{t}_{SB} (1 - \bar{r}'_T \bar{r}_{SB})^{-1} \bar{t}_T, \quad (11)$$

where $r_{SB}$ and $t_{SB}$ are calculated as

$$\bar{r}_{SB} = \bar{r}_B + \bar{t}'_B \bar{r}_S (1 - \bar{r}'_B \bar{r}_S)^{-1} \bar{t}_B, \quad \bar{t}_{SB} = \bar{t}_S (1 - \bar{r}'_B \bar{r}_S)^{-1} \bar{t}_B. \quad (12)$$

Here $r_B/t_B$ is the scattering matrix in the interfaces between substrate and sample and $r_S/t_S$ is the one between substrate and vacuum.

The Kerr signal can thus also depend on the substrate thickness $d_s$ when accounting for both the thickness and index of refraction ($n_s$) of the substrate, as illustrated in Fig. 6(a). The dependence of the Kerr and Faraday rotation angles on $d_s$ and $n_s$ are illustrated in Fig. 6(b) for the case of an optical frequency close to the gap (25 meV) and an electric field of 25 meV/nm. This $\mathcal{E}_z$ is smaller than the critical electric field, The substrate index of refractions in Fig. 6(b) are $n_s = 3$ a typical value for hexagonal boron nitride, $n_s = 5$ a typical value for silicon dioxide, and $n_s = 10$ a typical value of aluminum oxide. These results demonstrate explicitly that reflection off the substrate-vacuum interface is important whenever the light is not absorbed in the substrate. With the substrate thickness $d_s = 200\lambda$ as an example, the dependence of Kerr and Faraday rotations on the thickness of sample is plotted in Figs. 6(c) and 6(d), which is linearly proportional with the thickness of sample, and the slopes depend on the substrate index of refractions.

Finally, we examine the role of imperfect compensation between the half-quantized Hall conductivities on the top and bottom surfaces by fixing the difference of Hall conductivity between the two surfaces at $\sigma_T - \sigma_B = e^2/h$ and allowing

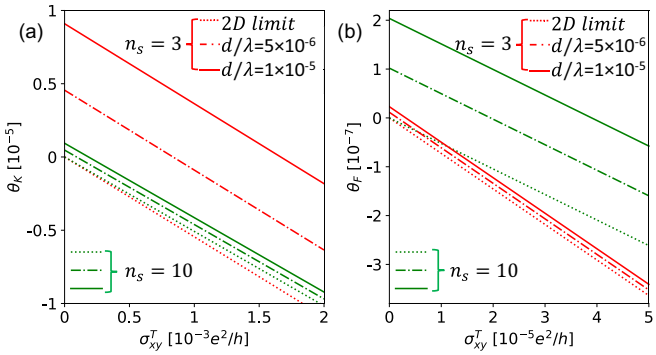


FIG. 7. Dependence of Kerr and Faraday angles on total Hall conductivity with substrate thickness set to $d_s = 0.56\lambda$. These results demonstrate additive linear dependence on $\sigma^T_{xy}$ and sample thickness $d$ that are distinctly different for substrate index of refraction $n_s = 3$ (red) and $n_s = 10$ (green).

the total to be nonzero. Our explicit calculations discussed previously have shown that the total Hall conductivity $\sigma^T_{xy}$ remains extremely small (as illustrated in Fig. 11) even for $\mathcal{E}_z \neq 0$ as long as the 2D system is an insulator. We do expect sizable conductivities to arise, however, when the Fermi level is in the local gap on one side of the film and not on the other. In Figs. 7(a) and 7(b), we plot the Kerr and Faraday angles versus $\sigma^T_{xy}$ for substrate thickness $d_s = 200\lambda$ for both $n_s = 3$ and $n_s = 10$. In each case, we plot results obtained using the 2D approximation and for the thicknesses of $N = 4$ and 8 septuple layer films. These calculations demonstrate that the Kerr and Faraday angles have additive linear contributions from both finite thickness and from a finite value of the total Hall conductivity of the film, and that both angles are sensitive to substrate properties.

## VI. DISCUSSION

$MnBi_2Te_4$ thin films with an odd number $N$ of septuple layers are two-dimensional insulating ferromagnets that exhibit the quantum anomalous Hall effect. Because they are ferromagnets with strong spin-orbit coupling, they have nonzero spin and orbital magnetizations in the absence of any external fields. Because they exhibit the quantum anomalous Hall effect, the films have large total optical Hall conductivities at frequencies below the gap that lead to substantial Kerr and Faraday effects that are readily observable and are indirectly related to the TME effect. In this paper, we focus on the magnetoelectric and magneto-optical response properties of even $N$ thin films, which are axion insulators. We find that although the dc magnetization response to electric field is quantized, the response of the magnetooptical Faraday and Kerr and angles to an electric field is extremely weak, and what survives might be difficult to disentangle. We predict that at frequencies below the gap, the Kerr and Faraday angles of realistic thin films will have additive small contributions from the finite thicknesses of the $MnBi_2Te_4$ samples, and from imperfect compensation between contributions to the total Hall conductivity from the top and bottom of the thin films. The best way to identify the TME, we believe, is to do it thermodynamically by measuring the temperature and magnetic-field dependent capacitance of hBN-encapsulated $MnBi_2Te_4$ thin films.

## ACKNOWLEDGMENT

This work was supported by the Department of Energy under Grant No. DE-SC0021984.

## APPENDIX A: OPTICAL CONDUCTIVITIES

The optical conductivities of AFM $MnBi_2Te_4$ thin films from $N = 1$ septuple layer to $N = 10$ septuple layers are illustrated in Fig. 8. The real and imaginary parts of $\sigma_{xx}(\omega)$ and $\sigma_{xy}(\omega)$ are plotted separately in Figs. 8(a)–8(d). In Figs. 8(a) and 8(b), we see that both the real and imaginary parts of $\sigma_{xx}(\omega)$ have typical interband absorption edge features at the $N$-dependent gap energy. The real and imaginary parts of $\sigma_{xy}(\omega)$ vanish identically for all even $N$ films, as shown in Figs. 8(a) and 8(b), due to the combined time-reversal times spacial inversion symmetry. The quantum anomalous Hall and trivial insulators are clearly distinguished by the Hall conductivities at frequencies well below the band gap.

For $MnBi_2Te_4$ thin films in the FM state, the frequency dependence of longitudinal optical conductivity $\sigma_{xx}(\omega)$ is similar to the ones in the AFM state. In Figs. 9(a) and 9(b), we show the plots of real and imaginary parts of $\sigma_{xx}(\omega)$ for $MnBi_2Te_4$ thin films with thickness from five SLs to ten SLs, the steplike behaviors of $\mathrm{Re}\sigma_{xx}(\omega)$ origin from the accumulated exited subbands when the frequency increases. The Hall conductivities, shown in Figs. 9(c) and 9(d), where we use the same color to label the same thickness as in Figs. 9(a) and 9(b), have different dependencies on optical conductivity compared with the AFM state. In the dc limit, a topological phase transition happens when the thickness increases to $N \geqslant 9$; above the critical thickness the Chern number increases from 1 to 2. $\mathrm{Im}\sigma_{xy}(\omega)$ shown in Fig. 9(d) indicates that the frequency

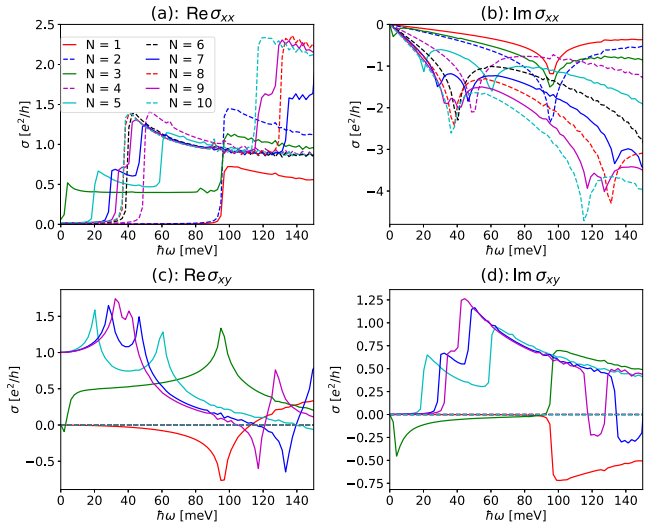


FIG. 8. Optical conductivity tensors of antiferromagnetic thin film with septuple layer numbers $N$ varying from 1 to 10. (a) Real parts of $\sigma_{xx}(\omega)$. (b) Imaginary parts of $\sigma_{xx}(\omega)$. (c) Real parts of $\sigma_{xy}(\omega)$. (d) Imaginary parts of $\sigma_{xy}(\omega)$. The same colors are used to label the $MnBi_2Te_4$ thickness in (b)–(d) as in (a).

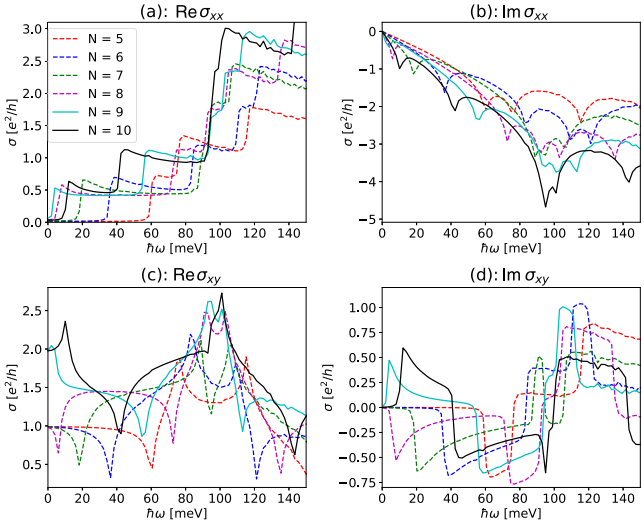


FIG. 9. Optical conductivities for ferromagnetic thin films with the number of layers from five to ten. (a) Real parts of $\sigma_{xx}(\omega)$. (b) Imaginary parts of $\sigma_{xx}(\omega)$. (c) Real parts of $\sigma_{xy}(\omega)$. (d) Imaginary parts of $\sigma_{xy}(\omega)$. In (c) and (d), the same colors as (a) are used to label the thickness of $MnBi_2Te_4$ thin films.

dependence differs between $N \geqslant 9$ and $N < 9$ thin films. Note that $\mathrm{Im}\sigma_{xy}(\omega) < 0$ at low frequencies for $N < 9$ thin films; this is due to the negative Berry curvature close to Γ point in 2D bands. The negative Berry curvature also leads to a decrease of $\mathrm{Re}\sigma_{xy}(\omega)$ shown in Fig. 9(c).

## APPENDIX B: ELECTRIC FIELD DEPENDENCE OF OPTICAL CONDUCTIVITY

In Fig. 10, the dependence of optical conductivities $\sigma_{xx}$ on electric field and frequency for four-layer AFM thin films are plotted.

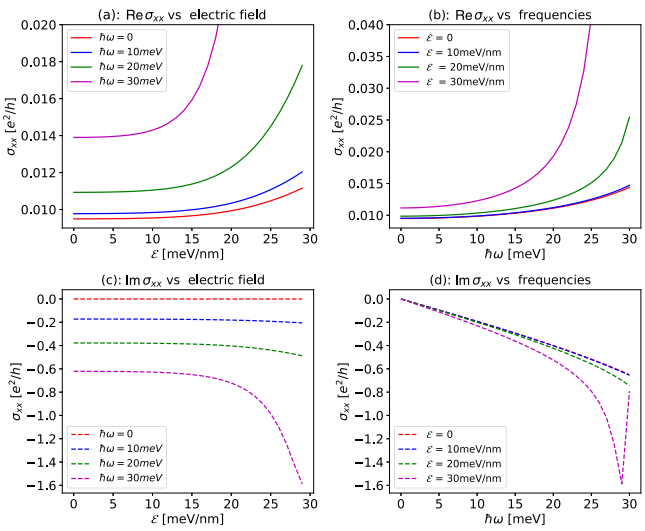


FIG. 10. Optical conductivities $\sigma_{xx}$ for four-layer antiferromagnetic thin film. (a) Real parts of versus electric field. (b) Real parts of $\sigma_{xx}$ versus optical frequencies $\omega$. (c) Imaginary parts of versus electric field. (d) Imaginary parts of versus optical frequencies $\omega$.

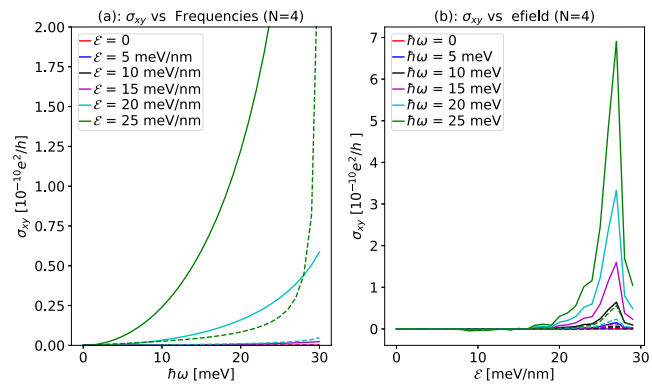


FIG. 11. Optical Hall conductivities $\sigma_{xy}$ for four-layer antiferromagnetic thin film. (a) Real and imaginary parts of $\sigma_{xy}$ versus optical frequencies $\omega$. (b) Real and imaginary parts of $\sigma_{xy}$ versus electric field.

The dependence of optical conductivities $\sigma_{xy}$ electric field and frequency are shown in Fig. 11.

In Figs. 12(a) and 12(b), we show a typical example of Faraday and Kerr rotation angles calculated in 2D limit for a typical even-layer thin films, i.e., $N = 4$ thin film in AFM state. From the plots, we see there is a maximized optical response around the critical electric field that drives the axion insulator state to a semimetal state, which is around 25 meV/nm for four-layer thin film, and when the frequencies exceed the band gap of $MnBi_2Te_4$ thin film, which is around 50 meV.

As a comparison, the Faraday and Kerr rotation angles in the 2D limit for $N = 5$ $MnBi_2Te_4$ thin film as an example of odd-layer case are shown in Figs. 12(c) and 12(d). We see that the Faraday rotation angles maximize at the dc limit in the absence of electric fields. In the presence of external field, the Faraday rotation angles decrease and minimize when the

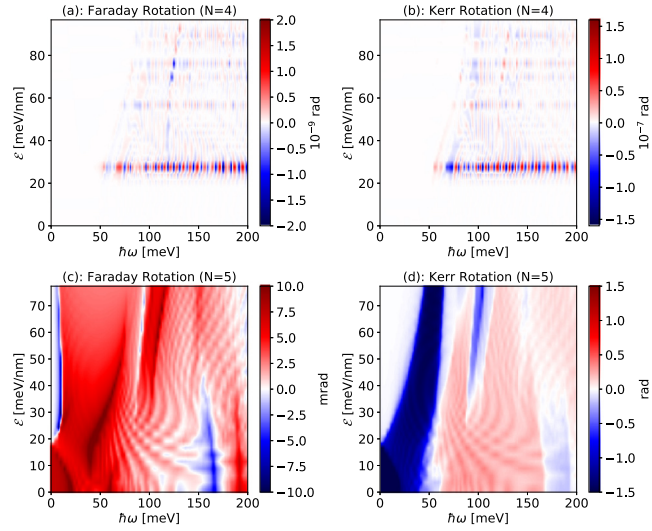


FIG. 12. Electric field dependence of Kerr and Faraday rotation for antiferromagnetic $MnBi_2Te_4$ thin films with thickness of four and five septuple layers. (a), (b) Plots of Faraday and Kerr rotation angles versus optical frequencies and external electric fields for $N = 4$ $MnBi_2Te_4$ thin film. (c), (d) Plots for $N = 5$ $MnBi_2Te_4$ thin film.

thin film is driven to a semimetal phase, i.e., at the electric field of around 20 meV/nm for five-layer thin film. Note that this critical field depends on the optical frequencies, that is, a positive dependence at low frequencies. Kerr rotation angles have similar dependence on electric field compared with Faraday rotation angles. The Faraday and Kerr rotation signals can thus be used as a detection of the topological phase transition induced by external electric fields.


[1] M. Z. Hasan and C. L. Kane, Colloquium: Topological insulators, Rev. Mod. Phys. **82**, 3045 (2010).

[2] X.-L. Qi and S.-C. Zhang, Topological insulators and superconductors, Rev. Mod. Phys. **83**, 1057 (2011).

[3] X.-L. Qi, T. L. Hughes, and S.-C. Zhang, Topological field theory of time-reversal invariant insulators, Phys. Rev. B **78**, 195424 (2008).

[4] A. M. Essin, J. E. Moore, and D. Vanderbilt, Magnetoelectric Polarizability and Axion Electrodynamics in Crystalline Insulators, Phys. Rev. Lett. **102**, 146805 (2009).

[5] A. M. Essin, A. M. Turner, J. E. Moore, and D. Vanderbilt, Orbital magnetoelectric coupling in band insulators, Phys. Rev. B **81**, 205104 (2010).

[6] K. Nomura and N. Nagaosa, Surface-Quantized Anomalous Hall Current and the Magnetoelectric Effect in Magnetically Disordered Topological Insulators, Phys. Rev. Lett. **106**, 166802 (2011).

[7] J. Wang, B. Lian, X.-L. Qi, and S.-C. Zhang, Quantized topological magnetoelectric effect of the zero-plateau quantum anomalous Hall state, Phys. Rev. B **92**, 081107(R) (2015).

[8] T. Morimoto, A. Furusaki, and N. Nagaosa, Topological magnetoelectric effects in thin films of topological insulators, Phys. Rev. B **92**, 085113 (2015).

[9] K. M. Fijalkowski, N. Liu, M. Hartl, M. Winnerlein, P. Mandal, A. Coschizza, A. Fothergill, S. Grauer, S. Schreyeck, K. Brunner, M. Greiter, R. Thomale, C. Gould, and L. W. Molenkamp, Any axion insulator must be a bulk three-dimensional topological insulator, Phys. Rev. B **103**, 235111 (2021).

[10] R. Chen, H.-P. Sun, and B. Zhou, Side-surface-mediated hybridization in axion insulators, Phys. Rev. B **107**, 125304 (2023).

[11] W.-K. Tse and A. H. MacDonald, Magneto-optical Faraday and Kerr effects in topological insulator films and in other layered quantized Hall systems, Phys. Rev. B **84**, 205327 (2011).

[12] W.-K. Tse and A. H. MacDonald, Giant Magneto-Optical Kerr Effect and Universal Faraday Effect in Thin-Film Topological Insulators, Phys. Rev. Lett. **105**, 057401 (2010).

[13] W.-K. Tse and A. H. MacDonald, Magneto-optical and magnetoelectric effects of topological insulators in quantizing magnetic fields, Phys. Rev. B **82**, 161104(R) (2010).

[14] L. Wu, M. Salehi, N. Koirala, J. Moon, S. Oh, and N. P. Armitage, Quantized Faraday and Kerr rotation and axion electrodynamics of a 3D topological insulator, Science **354**, 1124 (2016).

[15] V. Dziom, A. Shuvaev, A. Pimenov, G. Astakhov, C. Ames, K. Bendias, J. Böttcher, G. Tkachov, E. Hankiewicz, C. Brüne *et al.*, Observation of the universal magnetoelectric effect in a 3D topological insulator, Nat. Commun. **8**, 15197 (2017).

[16] N. P. Armitage, E. J. Mele, and A. Vishwanath, Weyl and Dirac semimetals in three-dimensional solids, Rev. Mod. Phys. **90**, 015001 (2018).

[17] N. P. Armitage and L. Wu, On the matter of topological insulators as magnetoelectrics, SciPost Phys. **6**, 046 (2019).

[18] Q. L. He, T. L. Hughes, N. P. Armitage, Y. Tokura, and K. L. Wang, Topological spintronics and magnetoelectronics, Nat. Mater. **21**, 15 (2022).

[19] C. Berger, F. Bayer, L. W. Molenkamp, and T. Kiessling, The topological Faraday effect cannot be observed in a realistic sample, arXiv:2212.04716.

[20] J. Ahn, S.-Y. Xu, and A. Vishwanath, Theory of optical axion electrodynamics and application to the Kerr effect in topological antiferromagnets, Nat. Commun. **13**, 7615 (2022).

[21] S. Ghosh, A. Sahoo, and S. Nandy, Theoretical investigations on Kerr and Faraday rotations in topological multi-Weyl semimetals, arXiv:2209.11217.

[22] L. Fu and C. L. Kane, Topological insulators with inversion symmetry, Phys. Rev. B **76**, 045302 (2007).

[23] C. Brüne, C. X. Liu, E. G. Novik, E. M. Hankiewicz, H. Buhmann, Y. L. Chen, X. L. Qi, Z. X. Shen, S. C. Zhang, and L. W. Molenkamp, Quantum Hall Effect from the Topological Surface States of Strained Bulk HgTe, Phys. Rev. Lett. **106**, 126803 (2011).

[24] D. A. Kozlov, Z. D. Kvon, E. B. Olshanetsky, N. N. Mikhailov, S. A. Dvoretsky, and D. Weiss, Transport Properties of a 3D Topological Insulator Based on a Strained High-Mobility HgTe Film, Phys. Rev. Lett. **112**, 196801 (2014).

[25] Y. Xu, I. Miotkowski, C. Liu, J. Tian, H. Nam, N. Alidoust, J. Hu, C.-K. Shih, M. Z. Hasan, and Y. P. Chen, Observation of topological surface state quantum Hall effect in an intrinsic three-dimensional topological insulator, Nat. Phys. **10**, 956 (2014).

[26] R. Yoshimi, A. Tsukazaki, Y. Kozuka, J. Falson, K. Takahashi, J. Checkelsky, N. Nagaosa, M. Kawasaki, and Y. Tokura, Quantum Hall effect on top and bottom surface states of topological insulator $(Bi_{1-x}Sb_x)_2Te_3$ films, Nat. Commun. **6**, 6627 (2015).

[27] R. Yu, W. Zhang, H.-J. Zhang, S.-C. Zhang, X. Dai, and Z. Fang, Quantized anomalous Hall effect in magnetic topological insulators, Science **329**, 61 (2010).

[28] C.-X. Liu, X.-L. Qi, X. Dai, Z. Fang, and S.-C. Zhang, Quantum Anomalous Hall Effect in $Hg_{1-y}Mn_yTe$ Quantum Wells, Phys. Rev. Lett. **101**, 146802 (2008).

[29] C.-Z. Chang, J. Zhang, X. Feng, J. Shen, Z. Zhang, M. Guo, K. Li, Y. Ou, P. Wei, L.-L. Wang, Z.-Q. Ji, Y. Feng, S. Ji, X. Chen, J. Jia, X. Dai, Z. Fang, S.-C. Zhang, K. He, Y. Wang *et al.*, Experimental observation of the quantum anomalous Hall effect in a magnetic topological insulator, Science **340**, 167 (2013).

[30] C. Lei, S. Chen, and A. H. MacDonald, Magnetized topological insulator multilayers, Proc. Natl. Acad. Sci. **117**, 27224 (2020).

[31] A. H. MacDonald, Introduction to the physics of the quantum Hall regime, arXiv:cond-mat/9410047v1.

[32] R. S. K. Mong, A. M. Essin, and J. E. Moore, Antiferromagnetic topological insulators, Phys. Rev. B **81**, 245209 (2010).

[33] C. Lei, O. Heinonen, A. H. MacDonald, and R. J. McQueeney, Metamagnetism of few-layer topological antiferromagnets, Phys. Rev. Mater. **5**, 064201 (2021).

[34] C. Lei, T. V. Trevisan, O. Heinonen, R. J. McQueeney, and A. H. MacDonald, Quantum anomalous Hall effect in perfectly compensated collinear antiferromagnetic thin films, Phys. Rev. B **106**, 195433 (2022).

[35] M. M. Otrokov, T. V. Menshchikova, M. G. Vergniory, I. P. Rusinov, A. Yu Vyazovskaya, Y. M. Koroteev, G. Bihlmayer, A. Ernst, P. M. Echenique, A. Arnau *et al.*, Highly-ordered wide bandgap materials for quantized anomalous Hall and magnetoelectric effects, 2D Mater. **4**, 025082 (2017).

[36] S. Eremeev, M. Otrokov, and E. Chulkov, Competing rhombohedral and monoclinic crystal structures in $MnPn_2Ch_4$ compounds: An ab-initio study, J. Alloys Compd. **709**, 172 (2017).

[37] M. M. Otrokov, I. I. Klimovskikh, H. Bentmann, D. Estyunin, A. Zeugner, Z. S. Aliev, S. Gaß, A. U. B. Wolter, A. V. Koroleva, A. M. Shikin *et al.*, Prediction and observation of an antiferromagnetic topological insulator, Nature (London) **576**, 416 (2019).

[38] M. M. Otrokov, I. P. Rusinov, M. Blanco-Rey, M. Hoffmann, A. Y. Vyazovskaya, S. V. Eremeev, A. Ernst, P. M. Echenique, A. Arnau, and E. V. Chulkov, Unique Thickness-Dependent Properties of the Van Der Waals Interlayer Antiferromagnet $MnBi_2Te_4$ Films, Phys. Rev. Lett. **122**, 107202 (2019).

[39] E. D. L. Rienks, S. Wimmer, J. Sánchez-Barriga, O. Caha, P. S. Mandal, J. Růžička, A. Ney, H. Steiner, V. V. Volobuev, H. Groiss *et al.*, Large magnetic gap at the dirac point in $Bi_2Te_3/MnBi_2Te_4$ heterostructures, Nature (London) **576**, 423 (2019).

[40] Y. J. Chen, L. X. Xu, J. H. Li, Y. W. Li, H. Y. Wang, C. F. Zhang, H. Li, Y. Wu, A. J. Liang, C. Chen, S. W. Jung, C. Cacho, Y. H. Mao, S. Liu, M. X. Wang, Y. F. Guo, Y. Xu, Z. K. Liu, L. X. Yang, and Y. L. Chen, Topological Electronic Structure and Its Temperature Evolution in Antiferromagnetic Topological Insulator $MnBi_2Te_4$, Phys. Rev. X **9**, 041040 (2019).

[41] H. Deng, Z. Chen, A. Wołoś, M. Konczykowski, K. Sobczak, J. Sitnicka, I. V. Fedorchenko, J. Borysiuk, T. Heider, Ł. Pluciński *et al.*, High-temperature quantum anomalous Hall regime in a $MnBi_2Te_4/Bi_2Te_3$ superlattice, Nat. Phys. **17**, 36 (2021).

[42] J. Ge, Y. Liu, J. Li, H. Li, T. Luo, Y. Wu, Y. Xu, and J. Wang, High-Chern-number and high-temperature quantum Hall effect without Landau levels, Natl. Sci. Rev. **7**, 1280 (2020).

[43] J. Li, Y. Li, S. Du, Z. Wang, B.-L. Gu, S.-C. Zhang, K. He, W. Duan, and Y. Xu, Intrinsic magnetic topological insulators in van der Waals layered $MnBi_2Te_4$-family materials, Sci. Adv. **5**, eaaw5685 (2019).

[44] S. Chowdhury, K. F. Garrity, and F. Tavazza, Prediction of Weyl semimetal and antiferromagnetic topological insulator phases in $Bi_2MnSe_4$, npj Comput. Mater. **5**, 33 (2019).

[45] B. Li, J.-Q. Yan, D. Pajerowski, E. Gordon, A.-M. Nedić, Y. Sizyuk, L. Ke, P. Orth, D. Vaknin, and R. McQueeney, Competing Magnetic Interactions in the Antiferromagnetic Topological Insulator $MnBi_2Te_4$, Phys. Rev. Lett. **124**, 167204 (2020).

[46] J.-Q. Yan, Q. Zhang, T. Heitmann, Z. Huang, K. Y. Chen, J.-G. Cheng, W. Wu, D. Vaknin, B. C. Sales, and R. J. McQueeney, Crystal growth and magnetic structure of $MnBi_2Te_4$, Phys. Rev. Mater. **3**, 064202 (2019).

[47] A. Zeugner, F. Nietschke, A. U. B. Wolter, S. Gaß, R. C. Vidal, T. R. F. Peixoto, D. Pohl, C. Damm, A. Lubk, R. Hentrich *et al.*, Chemical aspects of the candidate antiferromagnetic topological insulator $MnBi_2Te_4$, Chem. Mater. **31**, 2795 (2019).

[48] S. Zhang, R. Wang, X. Wang, B. Wei, B. Chen, H. Wang, G. Shi, F. Wang, B. Jia, Y. Ouyang *et al.*, Experimental observation of the gate-controlled reversal of the anomalous Hall effect in the intrinsic magnetic topological insulator $MnBi_2Te_4$ device, Nano Lett. **20**, 709 (2020).

[49] C. Liu, Y. Wang, H. Li, Y. Wu, Y. Li, J. Li, K. He, Y. Xu, J. Zhang, and Y. Wang, Robust axion insulator and Chern insulator phases in a two-dimensional antiferromagnetic topological insulator, Nat. Mater. **19**, 522 (2020).

[50] C. Lei and A. H. MacDonald, Gate-tunable quantum anomalous Hall effects in $MnBi_2Te_4$ thin films, Phys. Rev. Mater. **5**, L051201 (2021).

[51] R. Kubo, Statistical-mechanical theory of irreversible processes. I. General theory and simple applications to magnetic and conduction problems, J. Phys. Soc. Jpn. **12**, 570 (1957).

[52] D. A. Greenwood, The Boltzmann equation in the theory of electrical conduction in metals, Proc. Phys. Soc. **71**, 585 (1958).

[53] D. Xiao, J. Shi, and Q. Niu, Berry Phase Correction to Electron Density of States in Solids, Phys. Rev. Lett. **95**, 137204 (2005).

[54] D. Ceresoli, T. Thonhauser, D. Vanderbilt, and R. Resta, Orbital magnetization in crystalline solids: Multi-band insulators, Chern insulators, and metals, Phys. Rev. B **74**, 024408 (2006).

[55] T. Thonhauser, D. Ceresoli, D. Vanderbilt, and R. Resta, Orbital Magnetization in Periodic Insulators, Phys. Rev. Lett. **95**, 137205 (2005).

[56] J. Shi, G. Vignale, D. Xiao, and Q. Niu, Quantum Theory of Orbital Magnetization and Its Generalization to Interacting Systems, Phys. Rev. Lett. **99**, 197202 (2007).

[57] N. Pournaghavi, A. Pertsova, A. H. MacDonald, and C. M. Canali, Nonlocal sidewall response and deviation from exact quantization of the topological magnetoelectric effect in axion-insulator thin films, Phys. Rev. B **104**, L201102 (2021).

[58] J. Xia, Y. Maeno, P. T. Beyersdorf, M. M. Fejer, and A. Kapitulnik, High Resolution Polar Kerr Effect Measurements of $Sr_2RuO_4$: Evidence for Broken Time-Reversal Symmetry in the Superconducting State, Phys. Rev. Lett. **97**, 167002 (2006).

[59] A. Rowe, I. Zhaksylykova, G. Dilasser, Y. Lassailly, and J. Peretti, Polarizers, optical bridges, and Sagnac interferometers for nanoradian polarization rotation measurements, Rev. Sci. Instrum. **88**, 043903 (2017).